

Tree Tensor Network State with Variable Tensor Order: An Efficient Multireference Method for Strongly Correlated Systems

V. Murg,[†] F. Verstraete,^{†,#} R. Schneider,[‡] P. R. Nagy,^{§,||} and Ö. Legeza^{*,⊥}

[†]Fakultät für Physik, Universität Wien, Boltzmanngasse 3, A-1090 Vienna, Vienna, Austria

[‡]Technische Universität Berlin Fakultät II - Mathematik und Naturwissenschaften Institut für Mathematik, Strasse des 17. Juni 136, Berlin, Berlin, Germany

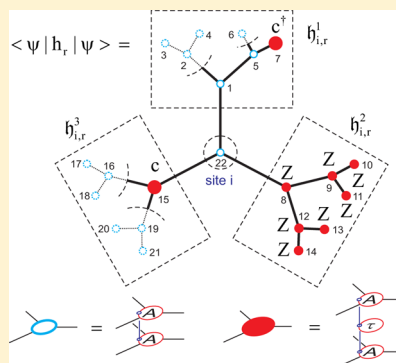
[§]Eötvös Loránd University, Budapest, Pázmány P. sétány 1/A, H-1117 Budapest, Hungary

^{||}MTA-BME Lendület Quantum Chemistry Research Group, Department of Physical Chemistry and Materials Science, Budapest University of Technology and Economics, P.O. Box 91, H-1521 Budapest, Hungary

[⊥]Strongly correlated systems "Lendület" research group, Wigner Research Centre for Physics, P.O. Box 49, H-1121 Budapest, Hungary

[#]Ghent University, Krijgslaan 281, Ghent, Belgium

ABSTRACT: We study the tree-tensor-network-state (TTNS) method with variable tensor orders for quantum chemistry. TTNS is a variational method to efficiently approximate complete active space (CAS) configuration interaction (CI) wave functions in a tensor product form. TTNS can be considered as a higher order generalization of the matrix product state (MPS) method. The MPS wave function is formulated as products of matrices in a multiparticle basis spanning a truncated Hilbert space of the original CAS-CI problem. These matrices belong to active orbitals organized in a one-dimensional array, while tensors in TTNS are defined upon a tree-like arrangement of the same orbitals. The tree-structure is advantageous since the distance between two arbitrary orbitals in the tree scales only logarithmically with the number of orbitals N , whereas the scaling is linear in the MPS array. It is found to be beneficial from the computational costs point of view to keep strongly correlated orbitals in close vicinity in both arrangements; therefore, the TTNS ansatz is better suited for multireference problems with numerous highly correlated orbitals. To exploit the advantages of TTNS a novel algorithm is designed to optimize the tree tensor network topology based on quantum information theory and entanglement. The superior performance of the TTNS method is illustrated on the ionic-neutral avoided crossing of LiF. It is also shown that the avoided crossing of LiF can be localized using only ground state properties, namely one-orbital entanglement.



I. INTRODUCTION

It has been more than a decade ago that the quantum chemistry version of the density matrix renormalization group (QC-DMRG) method^{1,2} has been applied to study the ionic-neutral curve crossing of LiF in order to demonstrate that it provides a globally accurate description of the system even if the wave function changes dramatically transversing the avoided crossing.³ In the following years, various theoretical studies have been devoted to investigate dissociation curves in diatomic molecules using QC-DMRG,^{4–8} and by now the method has become a rival to the conventional multiconfiguration wave function approaches.^{9–11} Inclusion of the concepts of entanglement from quantum information theory (QIT)^{12–15} has paved the road for identifying highly correlated molecular orbitals leading to an efficient construction of active spaces^{12,16} and for characterizing the various types of correlation effects relevant for chemical bonding.^{8,17}

In the mean time, a reformulation of DMRG in terms of so-called matrix product states (MPS)^{18–21} has shown that it is only one special case in a much more general set of methods:

the so-called tensor network states (TNS),^{19,22–32} which in certain cases is expected to even outperform QC-DMRG in the near future.^{33,34} A special form of TNS, the tree tensor network states (TTNS) approach,^{35–38} was first applied in quantum chemistry by some of us³³ to present the underlying theoretical background and scaling properties of the QC-TTNS algorithm, while an efficient extension of the two-site QC-DMRG using the tree-like topology has been applied recently to dendrimers.³⁴ In this latter work, a novel half-renormalization scheme has also been introduced in order to reduce computational cost related to the diagonalization of the effective Hamiltonian. The TTNS approach also plays a fundamental role in hierarchical tensor decompositions, recently developed for tensor product approximation,³¹ see e.g. refs 29 and 30.

Unlike models with translational symmetry studied usually in condensed matter physics, the orbital entanglement is non-

Received: December 30, 2014

Published: February 3, 2015

constant in the quantum chemical applications. Therefore, the optimal arrangement of matrices in MPS-based approaches has a tremendous effect on their performance and on the required computational resources to reach a given accuracy.^{12,15,39} Similar optimization strategies to find the best tensor topology are also crucial in the case of the TTNS algorithm.^{15,34}

In this paper, we discuss the most general version of the one-site QC-TTNS algorithm in which the local properties of the tensors can be different for each orbital. By studying the ionic-neutral potential curve crossing of the LiF we present an optimization strategy to set up tensor topologies which reflect the structure of the entanglement bonds between the molecular orbitals as the bond length between the Li and F is stretched. This problem is complicated enough to show that the optimization of the tree topology and the sweeping procedure is far from trivial and requires much more care than in the case of the QC-MPS. Therefore, we also compare the MPS-(DMRG) and TTNS convergence properties by changing the order of the tensors only. In our study, we calculate excited states as well, i.e., the two lowest $^1\Sigma^+$ states of LiF and the corresponding one- and two-orbital entropy functions.^{8,14} We use this example to demonstrate that the TTNS wave function is very stable even when the wave function changes dramatically transversing through an avoided crossing. The localization of the avoided crossing in terms of orbital entropy is also discussed.

The setup of the paper is as follows. In Section II we briefly describe the main steps of the QC-TTNS algorithm and the details of the numerical procedure used to determine the optimal tensor arrangements. Section III contains the numerical results and analysis of the observed trends of the numerical error. The summary of our conclusions is presented in Section IV.

II. NUMERICAL PROCEDURE

A. Hamiltonian and Target States. In the QC-DMRG and QC-TTNS applications, the electron–electron correlation is taken into account by an iterative procedure that minimizes the Rayleigh quotient corresponding to the Hamiltonian of the system:

$$H = \sum_{ij\sigma} T_{ij} c_{i\sigma}^\dagger c_{j\sigma} + \frac{1}{2} \sum_{ijkl\sigma\sigma'} V_{ijkl} c_{i\sigma}^\dagger c_{j\sigma}^\dagger c_{k\sigma} c_{l\sigma} \quad (1)$$

This Hamiltonian determines the exact states of the given molecule. In eq 1, $c_{i\sigma}^\dagger$ and $c_{j\sigma}$ create and annihilate an electron with spin σ , respectively. T_{ij} denotes the matrix elements of the one-particle Hamiltonian, which is comprised of the kinetic energy and the external electric field of the nuclei, and V_{ijkl} stands for the matrix elements of the electron repulsion operator, defined as

$$V_{ijkl} = \int d^3x_1 d^3x_2 \Phi_i^*(\vec{x}_1) \Phi_j^*(\vec{x}_2) \frac{1}{|\vec{x}_1 - \vec{x}_2|} \Phi_k(\vec{x}_2) \Phi_l(\vec{x}_1)$$

The matrix elements T_{ij} and V_{ijkl} are expressed in a molecular orbital (MO) basis obtained by CASSCF optimizations. The benchmark energies are computed with the same set of MO's. (For more details, see section Basis states.)

In the present version of our TTNS method non-Abelian symmetries^{40–44} are not implemented yet, thus in order to specify the eigenstates we have fixed the number of electrons with up and down spins and shifted the triplet levels from the low lying spectrum by adding a term $\sum_{i,j} \delta (S_i^+ S_j^- + S_i^- S_j^+)$ with S_i^+

$= c_{i\uparrow}^\dagger c_{i\downarrow}$ and $\delta = 1$ to the Hamiltonian given in eq 1. Nevertheless, we have also checked the total spin of each state by calculating the expectation value of the $S^2 = \sum_{ij} S_i^- S_j^+ + \sum_{ij} S_i^z S_j^z + \sum_i S_i^z$ operator which is equal to $S(S+1)$ in Hartree atomic units, i.e., zero for a singlet state and two for a triplet state.

In the MPS-based approaches, several eigenstates can be calculated within a single calculation. Therefore, we have formed the reduced density matrix of the target state, ρ , from the reduced density matrices of the lowest n eigenstates as $\rho = \sum_{\gamma} p_{\gamma} \rho_{\gamma}$ with $\gamma = 1 \dots n$ and $p_{\gamma} = 1/n$ at each bond length. In the case of our QC-DMRG code the orbital spatial symmetry of the target state can also be fixed³⁹ in which case the first two lowest lying $^1\Sigma^+$ states can be calculated directly by using only $n = 2$ eigenstates of the related subspace of the Hamiltonian. In the present version of our TTNS method, however, orbital spatial symmetry is not implemented yet. Therefore, we had to target the four lowest lying states with $n = 4$ due to the fact that there are two additional eigenstates between the two lowest $^1\Sigma^+$ states. For more detailed descriptions of target states we refer to the original works and reviews.^{1,3,45}

B. Basis States. Atomic orbital (AO) basis was adopted from the work of Bauschlicher and Langhoff⁴⁶ in order to match with previous DMRG computations.³ The AO basis set of ref. 46 is suitable to describe the ionic and covalent LiF states as well. It consists of 9s and 4p functions contracted to 4s and 2p functions on the Li atom and 9s, 6p, and 1d functions contracted to 4s, 3p, and 1d on the F atom. For more details of the AO basis set we refer to the original publication.⁴⁶

The two lowest $^1\Sigma^+$ states of LiF around the equilibrium bond length can be qualitatively described by the $1\sigma^2 2\sigma^2 3\sigma^2 4\sigma^2 1\pi^4$ and $1\sigma^2 2\sigma^2 3\sigma^2 4\sigma^1 5\sigma^1 1\pi^4$ configurations.⁴⁶ For this reason, the MO basis was obtained by CASSCF optimizations, with two active electrons on two active orbitals (4σ and 5σ) (CAS(2,2)). MO's were optimized simultaneously for both $^1\Sigma^+$ states. T_{ij} and V_{ijkl} matrix elements of eq 1 are expressed in this MO basis. CASSCF optimizations were carried out with the GAMESS-US quantum chemistry package.⁴⁷

Orbitals 1σ , 2σ , and 3σ were kept frozen in all presented configurational interaction (CI), MPS(DMRG), and TTNS computations. Six of the valence electrons were excited to all orbitals in the CI calculation, which we use as reference to compare the TTNS results to. Therefore, the active space in all CI, MPS(DMRG), and TTNS consists of 6 electrons and 25 orbitals: CAS(6,25). A smaller active space was also formulated for illustration purposes (Figure 11), that consists of 6 electrons and 18 orbitals: CAS(6,18). In this active space, besides the above-mentioned three occupied σ orbitals, the highest lying seven virtual orbitals were also kept frozen. CI results were obtained by utilizing the determinant-based full-configuration interaction (full-CI) program of Z. Rolik (Budapest), which is based on the CI algorithm of Olsen et al.⁴⁸ C_{2v} point group symmetry constraints were assigned during this study.

C. The QC-TTNS Method. In this section, we present the brief overview of the most general QC-TTNS algorithm. For the full description of the method we refer to the original work.³³ In our implementation, we allow tensors to have orbital dependent coordination number, z_{ij} , in contrast to the implementation of Nakatani et al.³⁴ which is an efficient extension of the DMRG method using fixed number of blocks. Our main motivation is to develop an algorithm which reflects the entanglement structure of the molecule under study as

much as possible (see Figure 9). The computational cost in one step of the algorithm scales as D_i^{z+1} where D is the dimension of the auxiliary space (in the DMRG community referred as block states), while the long-range correlation deviates from the mean-field value only polynomially with distance. Therefore, there is a trade-off between entanglement localization and increased order of the tensors. The construction of the optimal tensor network is thus a far more complex task than it is in the case of the MPS based approaches.

In a full-CI treatment, a given eigenfunction of eq 1 can be written in a full tensor form as

$$|\Psi\rangle = \sum_{\alpha_1, \dots, \alpha_N} U_{\alpha_1 \dots \alpha_N} |\alpha_1, \dots, \alpha_N\rangle \quad (2)$$

where $U_{\alpha_1 \dots \alpha_N}$ is a tensor with order N , and $|\alpha_i\rangle$ represents basis states at molecular orbital i . In our study, a molecular orbital can be empty, singly occupied with up or down spins, or doubly occupied, thus the dimension of the local Hilbert space, d , is four. Since the number of independent parameters in U scales exponentially with N it is mandatory to approximate such high dimensional tensor with a proper factorization in terms of lower dimensional tensors. In the MPS representation, U describes a matrix network, i.e., it emerges from contractions of a set of matrices $\{A^1, \dots, A^N\}$, where

$$A^i[\alpha_i]_{m_{i-1}, m_i} \quad (3)$$

is a matrix at each vertex i of the network, with 2 virtual indices m_{i-1}, m_i of dimension D and one physical index α_i of dimension d , thus

$$|\Psi\rangle = \sum_{\alpha_1, \dots, \alpha_N} A_{\alpha_1}^1 A_{\alpha_2}^2 \dots A_{\alpha_N}^N |\alpha_1\rangle |\alpha_2\rangle \dots |\alpha_N\rangle \quad (4)$$

The schematic plot of the matrix product state (MPS) network is shown in Figure 1.

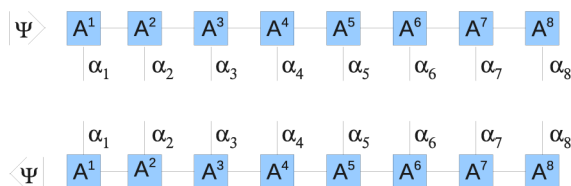


Figure 1. Schematic plot of the matrix product state (MPS) algorithm. Each node is represented by a tensor of order 2 and the vertical line the physical index α .

A natural extension of the MPS approach is to use higher order tensors. In this work, we form a tree tensor network in which all sites in the tree represent physical orbitals and in which entanglement is transferred via the virtual bonds that connect the sites as shown in Figure 2.

Our motivation is to treat models in which orbitals have varying degrees of entanglement; positions closer to the center of the tree should be better suited to represent more entangled sites. An additional motivation is to take advantage of the property of the tree tensor network ansatz that the long-range correlations differ from the mean-field value polynomially with distance rather than exponentially with distance as for MPS. In our algorithmic approach to optimize the tree tensor network, we use tools similar to those used in refs 35, 36, 37, and 38 and optimize the network site-by-site as in the DMRG. Therefore,

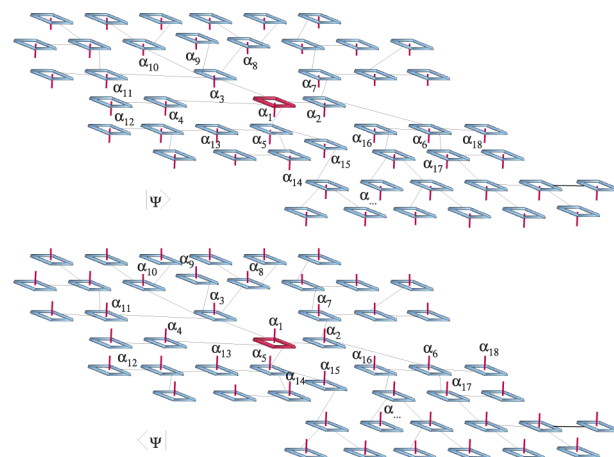


Figure 2. Schematic plot of a higher dimensional network, for example, the tree tensor network state (TTNS) algorithm. Each node is represented by a tensor of order z_i , where z_i is an orbital dependent coordination number. The network supposed to reflect the entanglement structure of the molecule as much as possible. The vertical red lines denote physical indices $\alpha_i, i \in \{1, N\}$. Entanglement is transferred via the virtual bonds that connect the orbitals shown by black lines. The central node is indicated by red contour.

$U_{\alpha_1 \dots \alpha_N}$ can describe a tree tensor network, i.e., they emerge from contractions of a set of tensors $\{A_1, \dots, A_N\}$, where

$$A^i[\alpha_i]_{m_1 \dots m_z} \quad (5)$$

is a tensor with $z + 1$ indices, at each vertex i of the network according to Figure 3. Each tensor has z virtual indices $m_1 \dots m_z$

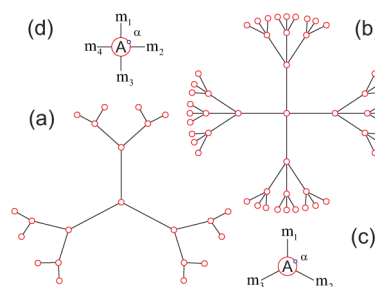


Figure 3. Top view of the tree tensor network (TTNS) algorithm with fixed coordination number, (a) $z_i = 3$ and (b) $z_i = 4$. The structure of the tensors is shown in (c) and (d). The bonds indicate the virtual indices m_1, \dots, m_z and the circle the physical index α .

of dimension D and one physical index α_i of dimension d , with z being the coordination number of that site. The coefficients $U_{\alpha_1 \dots \alpha_N}$ are obtained by contracting the virtual indices of the tensors according to the scheme of a tree tensor network (see Figure 3). The structure of the network can be arbitrary, and the coordination number can vary from site to site. The only condition is that the network is bipartite, i.e., by cutting one bond, the network separates into two disjoint parts. Therefore, the TTNS network does not contain any loop (see Figure 3) which allows an exact mathematical treatment.^{29,31} For $z = 2$, the one-dimensional MPS-ansatz used in DMRG is recovered.

Since entanglement is transferred via the virtual bonds that connect the sites, it is preferable to put strongly correlated sites close together, i.e. to minimize the number of bonds between them. For $z > 2$ the number of virtual bonds required to

connect two arbitrary orbitals scales logarithmically with the number of orbitals α , whereas the scaling is linear in N for $z = 2$. This can be seen by considering a Cayley-tree of depth Δ , as shown in Figure 3. The number of sites in the tree is

$$N = 1 + z \sum_{j=1}^{\Delta} (z-1)^{j-1} = \frac{z(z-1)^{\Delta} - z}{z-2}$$

and thus, the maximal distance between two orbitals, 2Δ , scales logarithmically with N for $z > 2$. Because of this logarithmic scaling, the expectation value of a long-range correlations differs from the mean-field result by a quantity that scales polynomially with distance. This contrasts the MPS ansatz ($z = 2$) that shows an exponential decay of the difference with distance.³³

The TTNS algorithm consists in the variational optimization of the tensors A_i in such a way that the energy is minimized (with the constraint that the norm of the state remains constant). This is equivalent to optimizing the functional

$$F = \langle \Psi | H | \Psi \rangle - E(\langle \Psi | \Psi \rangle - 1)$$

where $\Psi = \Psi(A_1, \dots, A_N)$. This functional is nonconvex with respect to all parameters $\{A_1, \dots, A_N\}$. However, fixing all tensors A_k except A_i due to the tensor network structure of the ansatz, it is quadratic in the parameters A_i associated with one lattice site i . Because of this, the optimal parameters A_i can simply be found by solving a generalized eigenvalue problem $\mathcal{H}_i \vec{A}_i = E \mathcal{N}_i \vec{A}_i$. For a bipartite network, it is always possible to assume a gauge condition so that $\mathcal{N}_i = 1$ and thus reduce the generalized eigenvalue problem to an ordinary one.³³ The concept of the algorithm is to do this one-site optimization site-by-site until convergence is reached. The challenge that remains is to calculate the effective Hamiltonian \mathcal{H}_i of the eigenvalue problem. In principle, this is done by contracting all indices in the expression for the expectation value $\langle \Psi | H | \Psi \rangle$ except those that connect to A_i . By interpreting the tensor A_i as a qD^z -dimensional vector \vec{A}_i , this expression can be written as $\langle \Psi | H | \Psi \rangle = \vec{A}_i^\dagger \mathcal{H}_i \vec{A}_i$. Since $\langle \Psi | \Psi \rangle = \vec{A}_i^\dagger \mathcal{N}_i \vec{A}_i$ and $\mathcal{N}_i = 1$, the functional F attains its minimum when

$$\mathcal{H}_i \vec{A}_i = E \vec{A}_i$$

Due to the bipartite structure of the tensor network, the calculation of \mathcal{H}_i can be performed efficiently, i.e., on a time that scales polynomially with N and D .

This TTNS algorithm is similar to a DMRG calculation with z blocks instead of two, where a block consists of all of the sites within one of the branches emerging from site i (see Figure 4(a)). The wave function is then formed as

$$|\Psi\rangle = \sum_{m_1, \dots, m_z=1}^D |\phi_{m_1, \dots, m_z}^i\rangle \otimes |\varphi_{m_1}^1\rangle \otimes \dots \otimes |\varphi_{m_z}^z\rangle \quad (6)$$

where $|\phi_m^i\rangle$ ($m = 1, \dots, D$) is the basis in environment block γ ($\gamma = 1, \dots, z$) and $|\varphi_{\alpha_i, \dots, \alpha_z}^i\rangle$ is the state of site i . Matrix \mathcal{N}_i is equal to the identity if the basis $|\phi_m^i\rangle$ in each environment block is orthonormal. This can always be achieved, because of a gauge degree of freedom in a TTNS;^{21,33,49} it is possible to insert at any bond a resolution of the identity $1 = VW$ and contract the matrices V and W with the adjacent tensors A_i (see Figure 4b). This does not change the state but changes the tensors A_i and the basis states $|\phi_m^i\rangle$ of the environment blocks. It can be shown

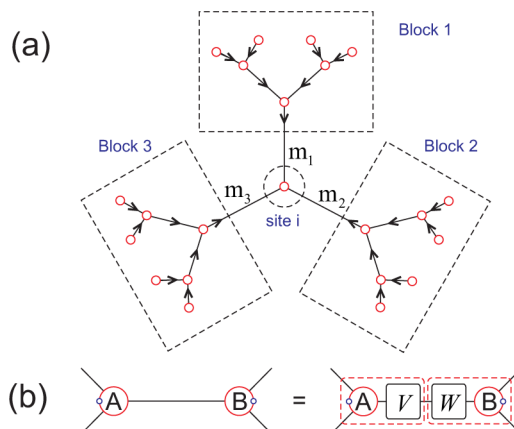


Figure 4. (a) Separation of the state into z blocks plus the site under optimization, as described by eq 6. (b) Natural freedom in the tensor network: insertion of a matrices V and W fulfilling $VW = 1$ at one bond leaves the state invariant. The contraction of A with V forms the new tensor A' on the left-hand side; the contraction of B with W forms the new tensor B' at the right-hand side.

that it is always possible to find gauge transformations that orthonormalize the basis states of the environment blocks.³³

Thus, by assuring that the gauge condition is always satisfied in the course of the algorithm, the only term that must be calculated is the effective Hamiltonian \mathcal{H}_i . This term is obtained by contracting all tensors except A_i in the expectation value $\langle \Psi | H | \Psi \rangle$ as shown in Figure 6. Indices $(\tilde{\alpha}_\gamma, \tilde{m}_i)$ form the row indices and (α_γ, m_i) the column indices of \mathcal{H}_i , such that

$\langle \Psi | H | \Psi \rangle = \vec{A}_i^\dagger \mathcal{H}_i \vec{A}_i$ is fulfilled. Hamiltonian H is a sum of $O(N^4)$ two-point and four-point Fermionic interaction terms $c_{i\sigma}^\dagger c_{j\sigma}$ and $c_{i\sigma}^\dagger c_{j\sigma'}^\dagger c_{k\sigma'} c_{l\sigma}$ ($\sigma, \sigma' \in \{\uparrow, \downarrow\}$), as defined in eq 1. The Fermionic nature of the terms can be handled by mapping them to nonlocal bosonic operators via Jordan-Wigner transformations. Writing $H = \sum_r h_r$ with h_r denoting the Jordan-Wigner transformed two- and four-point interaction terms, the effective Hamiltonian \mathcal{H}_i transforms into a sum $\mathcal{H}_i = \sum_r h_{i,r}$, where

$$\langle \Psi | h_r | \Psi \rangle = \vec{A}_i^\dagger \mathbf{h}_{i,r} \vec{A}_i$$

Due to the structure (6) of the TTNS, each effective Hamiltonian $\mathbf{h}_{i,r}$ factorizes into a tensor product of z matrices

$$\mathbf{h}_{i,r} = \mathbf{h}_{i,r}^1 \otimes \dots \otimes \mathbf{h}_{i,r}^z$$

where each matrix $\mathbf{h}_{i,r}^\gamma$ corresponds to the matrix elements of h_i with respect to the basis in environment block γ :

$$[\mathbf{h}_{i,r}^\gamma]_{mn} = \langle \phi_m^\gamma | h_r | \phi_n^\gamma \rangle$$

Graphically, the evaluation of $\langle \phi_m^\gamma | h_r | \phi_n^\gamma \rangle$ corresponds to the contraction of a three-layered tensor network according to the structure of the branch in block γ , as depicted in Figure 5. This network can be contracted efficiently by starting from the leaves and working in the inward direction.

With TTNS we can easily enforce the $U(1)$ symmetry that is fulfilled by Hamiltonian (1), i.e. the conservation of the number of particles. For this, the tree graph has to be made directed (see Figure 4a), such that all sites (except site i that is optimized) have $z-1$ incoming and one outgoing bond. Thus, each virtual index of a tensor A_i is equipped with the additional information on whether it is “incoming” or “outgoing”. Each

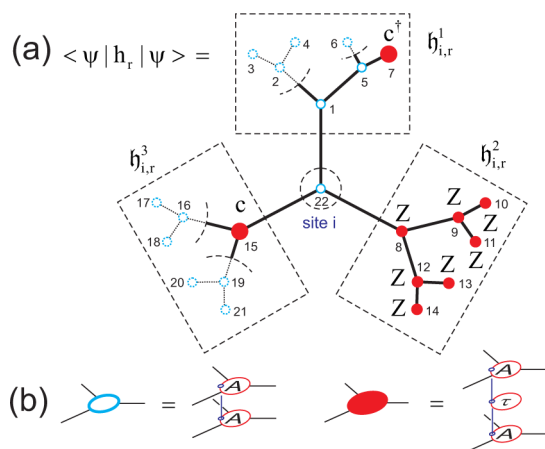


Figure 5. Formation of the effective Hamiltonian $h_{i,r} = h_{i,r}^1 \otimes h_{i,r}^2 \otimes h_{i,r}^3$ with respect to the Fermionic interaction $h_r = c_7^\dagger c_{15}$. Between sites 7 and 15 a chain of Z -matrices appears due to the Jordan-Wigner transformation. The sites on which the interaction has support are marked in red. Each open (filled) circle in the tensor network corresponds to the contraction of the layered structure of tensors shown in (b).

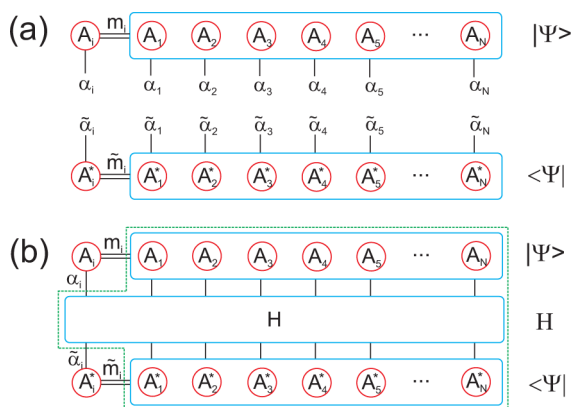


Figure 6. Construction of the effective Hamiltonian with respect to site i . (a) Ket- and Bra-TTNS with tensor A_i singled out. A_i has physical index α_i and connects with its virtual indices m_i to the remaining network with tensors A_1, \dots, A_N indicated by the blue box. (b) Expectation value $\langle \Psi | H | \Psi \rangle$ with respect to the TTNS written in (a). The effective Hamiltonian \mathcal{H}_i is obtained by contracting all tensors except A_i (the tensors surrounded by the green polygon).

virtual index connecting to block γ ($\gamma = 1, \dots, z$) is split into an index tuple $(m_\gamma, n_\gamma^\uparrow, n_\gamma^\downarrow)$. Assuming that the index connecting to block $\gamma = 1$ is the outgoing index, we require that $n_1^\uparrow = n_2^\uparrow + \dots + n_z^\uparrow + n^\uparrow(\alpha)$ and $n_1^\downarrow = n_2^\downarrow + \dots + n_z^\downarrow + n^\downarrow(\alpha)$. $n^\uparrow(\alpha)$ ($n^\downarrow(\alpha)$) denotes the number of electrons with spin up (down) corresponding to the physical index α . Thus, for $\gamma = 2, \dots, z$, n_γ^\uparrow (n_γ^\downarrow) counts the number of up-electrons (down-electrons) within branch γ . The index n_1^\uparrow (n_1^\downarrow), on the other hand, is equal to the number of electrons with spin up (down) in all the branches plus the number of electrons at site i .

Besides the ability of targeting a state with a specific total number of up- and down-electrons N_\uparrow and N_\downarrow utilization of symmetries also gives a performance boost to the algorithm since the virtual dimension effectively increases from D to $D(N_\uparrow + 1)(N_\downarrow + 1)$, and even further if spatial symmetry is also utilized. As an example, for the problem considered in the paper $D = 4$ would correspond to $M = 64$ DMRG block states.

Furthermore, if spatial symmetry is also exploited this increases to $M = 256$ in the C_{2v} point group. In addition, the inclusion of the particle-number conservation also simplifies the treatment of the Fermionic nature of the electrons. The main idea is depicted in Figure 7 for the interaction $c_7^\dagger c_{15}$: with an

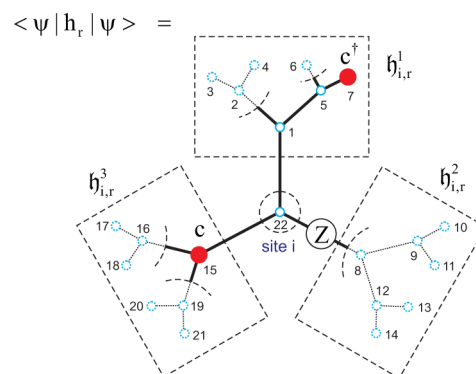


Figure 7. Formation of the effective Hamiltonian $h_{i,r} = h_{i,r}^1 \otimes h_{i,r}^2 \otimes h_{i,r}^3$ with respect to the Fermionic interaction $h_r = c_7^\dagger c_{15}$ with particle number conservation taken into account. The sites on which the interaction has support are marked in red. All branches marked by dotted lines and circles yield the identity when contracted. The parity operator \tilde{Z} is contracted to the virtual bond.

appropriately chosen numbering of the Fermions, each sub-branch that has no Fermionic support either has only identities acting on the sites or only matrices Z stemming from the Jordan-Wigner transformation ($Z_{ab} = \delta_{ab}(-1)^{n^\uparrow(a)+n^\downarrow(a)}$). The sub-branches including only identities simplify to the identity because we work in a gauge in which the basis in each environment block is orthonormal. As shown in ref 33, the Z operators can be “moved” to the virtual bonds and, since $Z^2 = 1$, all of them except one cancel (see Figures 5 and 7). What remains is a sub-branch that includes only identities, which reduces to the identity because of the orthonormalization of the state. Thus, for a Fermionic two-site interaction, it is sufficient to take into account the path connecting the two sites. In this way, the treatment of long-range Fermionic interactions is feasible with the same numerical effort as the treatment of long-range spin interactions.

The numerical effort of the algorithm has two major contributions. On the one hand, the bond-dimension (tensor rank) D is crucial: the numerical effort for calculating one term of the effective Hamiltonian by tensor contraction scales as D^{z+1} . On the other hand, this calculation has to be performed for each term in the Hamiltonian, such that naively a scaling $N^4 D^{z+1}$ is expected. Fortunately, the same summation tricks as described in refs 2 and 50 can be applied, such that the scaling reduces to $N^2 D^{z+1}$. Since $O(N)$ iteration steps are required for convergence, the overall time of the algorithm will scale as $N^3 D^{z+1}$. Therefore, in general tensor ranks decrease by going from MPS to TTNS, but the order of the tensors increases. However, the number of tensors with $z = 1$ lying on the boundary of the network increases exponentially when larger and larger systems are considered, and there is an expected crossover in CPU time between the full sweep of the MPS and TTNS. It is worth mentioning that if $D \geq d$, orbitals lying on the boundary are excluded automatically from the optimization.

D. Network Optimization by Entanglement Localization. The amount of contribution to the total correlation energy of an orbital can be detected qualitatively by the single-

orbital entropy, $s_i = -\text{Tr} \rho_i \ln \rho_i$ where ρ_i is the reduced density matrix at orbital i . The two-orbital entropy is constructed similarly using the reduced density matrix, ρ_{ij} , of a subsystem built from orbitals i and j , and the mutual information $I_{ij} = s_{ij} - s_i - s_j$ describes how orbitals are entangled with each other as they are embedded in the whole system. For more detailed derivations we refer to the original papers.^{8,12,14,15} Therefore, these quantities provide chemical information about the system, especially about bond formation and nature of static and dynamic correlation.^{8,16,17,51} As an example, s_i and I_{ij} are shown in Figures 8 and 9, respectively, for the equilibrium bond length

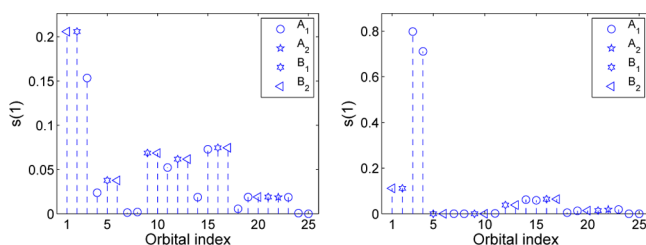


Figure 8. One orbital entropy profile for the LiF molecule at bond length (a) $r = 3.05$ and at (b) $r = 13.7$. Symbols label the irreducible representations of the molecular orbitals in the C_{2v} point group.

$r = 3.05$ and at large separation $r = 13.7$. The total quantum information encoded in the wave function is given by the sum of the orbital entropy, i.e., $I_{\text{tot}} = \sum_i s_i$, which is twice as large for the stretched geometry as compared to the equilibrium case.

It is clear from Figure 9 that some orbitals are strongly entangled with several other orbitals, while some orbitals are

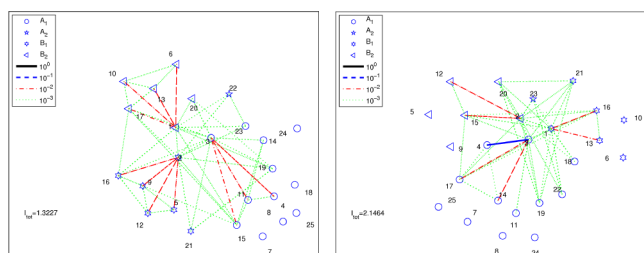


Figure 9. Mutual information represented as a two-dimensional weighted graph for the LiF molecule at bond length (a) $r = 3.05$ and at (b) $r = 13.7$. Colors indicate different strengths of I_{ij} , and the symbols label the irreducible representations of the molecular orbitals in the C_{2v} point group.

entangled with only a few others and some are almost disentangled from the system. Therefore, the obvious choice is to allow the coordination number, z_i , to vary from orbital to orbital. In the following analysis, however, we restrict ourselves to a fixed $z_i = 3$ case in order to allow a more direct analysis when data are compared to the $z_i = 2$ MPS case.

Since both DMRG and TTNS rely on the systematic application of the Schmidt-decomposition, the required computational resources to reach a given error margin is determined by the amount of entanglement in the system.³⁹ This can be manipulated by changing the basis functions^{33,52} or by changing the tensor topology. For the latter case, the entanglement length

$$\text{Cost}_\eta = \sum_{ij} I_{ij} \times d_{ij}^\eta \quad (7)$$

should be minimized in order to localize the entanglement in the system, where d_{ij} is the distance function between orbital i and j depending on the tensor topology, and η is some exponent that we set to 1 or 2. For the one-dimensional case, i.e., for DMRG and MPS $d_{ij} = |i - j|$. For the tree topology d_{ij} can be computed as the distance from the center to i , plus the distance from the center to j , minus twice the distance from the center to their lowest common ancestor. The lowest common ancestor can be obtained within a linear preprocessing time $O(N)$ and a constant query time using the Berkman's algorithm.⁵³ As an example, the optimized tensor topologies at the equilibrium bond length $r = 3.05$ are shown in Figure 10 for the one-dimensional topology and for the tree topology.

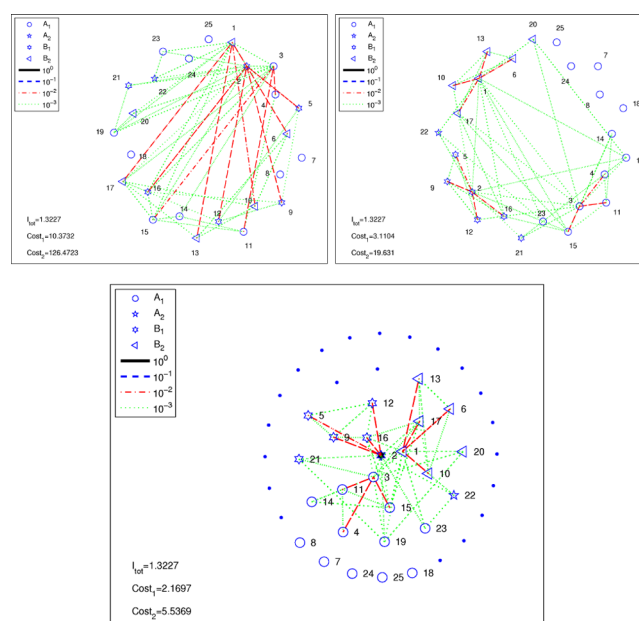


Figure 10. Optimization of tensor topology by minimizing the entanglement length in the system at the equilibrium bond length $r = 3.05$. (a) and (b) are for the one-dimensional MPS like topology for the original ordering and for the optimized ordering, respectively. (c) Shows the optimized topology on the tree (small dots indicate not used grid points of the tree). The total quantum information I_{tot} does not change, but the entanglement length calculated with $\eta = 1$ and 2 indicated by Cost_1 and Cost_2 drops significantly.

In practice, first we performed a quick and fast DMRG full sweep with a fixed small number of block states ($M \approx 16, \dots, 64$) using the ordering of orbitals for which the T_{ij} and V_{ijkl} integral files were generated by the GAMESS-US program in order to determine the one- and two-orbital entropy profiles qualitatively. For all subsequent calculations we rendered orbitals with descending orbital entropy values to form the Complete Active Space CAS-vector that was used during the configuration interaction based dynamic extended active space (CI-DEAS) procedure.¹² We also determined the mutual information, I_{ij} , and the orbitals were reordered by minimizing the entanglement length given by eq 7. In the one-dimensional case either the graph Laplacian can be used or by other heuristic methods to reduce the spectral envelope of I_{ij} , i.e., to make it as diagonally dominant as possible.^{54,55} In the case of the tree network, the optimization is less straightforward, but as a rule of thumb we placed orbitals with largest entropy values close to the center of the network while keeping orbitals with large I_{ij} values close together (see Figure 10(c)). In the

subsequent step, accurate DMRG (with optimized CAS vector) or MPS/TTNS calculations were performed.

III. NUMERICAL RESULTS

In this work we have used two codes. Our QC-DMRG program has been developed for a long time, and it includes advanced features like the dynamic block state selection (DBSS) approach,^{13,39} the CI-DEAS procedure,¹² and the treatment of orbital spatial symmetries which are not implemented yet in the TTNS code. Therefore, the entropy functions were calculated by the QC-DMRG code to provide initial data quickly for network optimizations.

A. Variable Tensor Orders and Convergence Properties. In order to present a more systematic analysis on the separated and combined effects of the network optimization with orbital dependent coordination number and the permutation of the orbital ordering in a given network, we calculated the ground state energy of CAS(6,18) with $D = 4$ for three different network topologies shown in Figure 11. Gradual increase in the rate of convergence can be achieved by optimizing the number of components with $z_i = 3$ together with the ordering of the orbitals in that given network topology as it is shown in Figure 11(d).

B. Ground State and Excited States. The rest of the analysis for a fair treatment is based on the TTNS code alone using fixed $z_i = 2$ (MPS) and $z_i = 3$ (TTNS) coordination number (except for the boundaries) while keeping all other parameters of the algorithm the same.

The potential energy curve (PES) can be calculated for an a priori set error margin using the DBSS procedure.³ Therefore, we have easily reproduced the full-CI energies up to 10^{-8} au in absolute error. In the following, however, we have used a small fixed number of block states, i.e., fixed bond dimension, in order to demonstrate the benefits underlying the TTNS geometry. The four lowest lying eigenstates ($\gamma = 1, \dots, 4$) are shown in Figure 12 calculated by the QC-DMRG method using $M = 64$ block states or alternatively by the TTNS approach with $z_i = 2$ and $D = 4$. We have confirmed that each state is a singlet with $S^2 = 0$.

The relative error of the ground state ($\gamma = 1$) and the third excited state ($\gamma = 4$), $\Delta E_\gamma = |E_\gamma - E_{\text{FCI}}|/E_{\text{FCI}}$, are shown in Figure 13. The open symbols stand for the MPS solution, while the filled symbols indicate the TTNS result. It is clear from the figure that the accuracy of the energy dropped for both states by at least an order of magnitude. For the ground state close to the equilibrium bond length the change is almost 2 orders of magnitude. It is important to emphasize again that all parameters of the calculations were kept fixed except that we used the optimized one-dimensional MPS-like topologies or the two-dimensional optimized TTNS-like topologies. The network topologies for both cases were optimized for each bond length using the procedure outlined in Section II.

In the MPS based DMRG method the matrices of the one-dimensional tensor network are optimized iteratively by traversing through the network starting from the left boundary until the right boundary is reached. In the following steps the same procedure is repeated but in the reverse direction. This systematic optimization procedure is called as sweeping. The relative error of the two $1^1\Sigma^+$ states as a function of iteration steps is shown in Figure 14 for the MPS case with $z_i = 2$ and $D = 4$. It can be seen in the figure that the relative error of the ground state energy drops quickly as a function of iteration steps, and it saturates after some 20 iterations. In contrast to

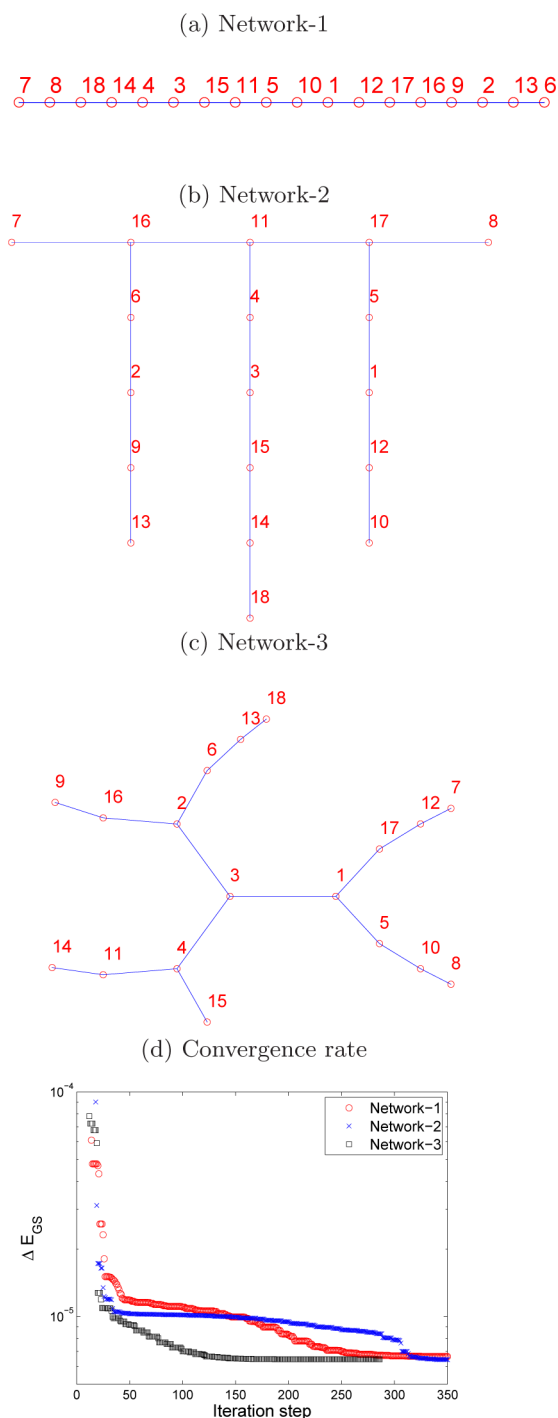


Figure 11. The ground state energy for LiF CAS(6,18) with $D = 4$ at $r = 3.05$ for three different network topologies using orbital dependent coordination numbers.

this, the convergence of the third excited state is somewhat slower. In addition, the method lost the target state for certain interaction steps, i.e., for certain network configurations. This is due to the very low bond dimension used in the test calculations. When we used larger bond dimension or included point group symmetries, this problem was fully eliminated.

In the case of the tree-network, there is more freedom to choose the optimal sweeping procedure, i.e., to choose the optimal path through which the network is traversed. In the present work, we have swept through the network by going

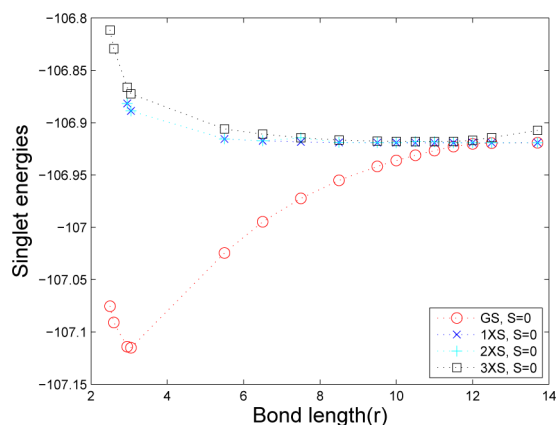


Figure 12. The energy of the four lowest lying states as a function of bond length.

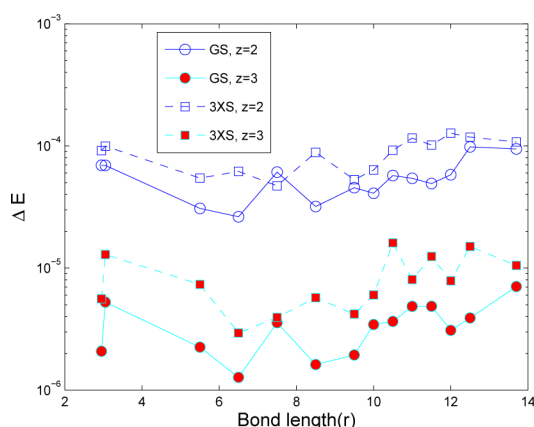


Figure 13. The relative error of the energy of the two lowest lying $^1\Sigma^+$ states as a function of bond length using the Tree-TNS with $z = 2$ and $z = 3$ with $D = 4$. For $z = 2$, the one-dimensional MPS-ansatz used in DMRG is recovered.

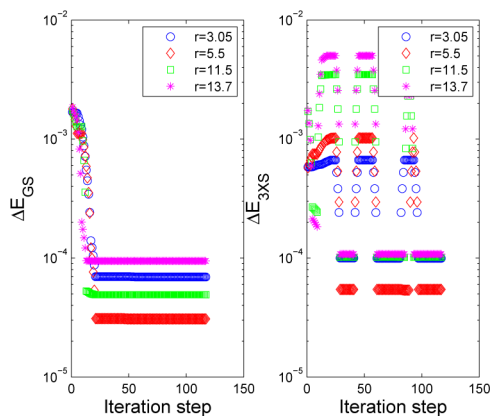


Figure 14. The relative error of the energy of the ground state and the third excited state as a function of iteration step with $z_i = 2$ and $D = 4$ for a few selected bond lengths.

recursively back and forth through each branch. Therefore, according to the labeling of the orbitals on the lattice shown in Figure 15 one sweep goes through the orbitals as 1 2 3 4 5 4 6 4 3 7 8 7 3 2 9 10 9 11 9 2 1 12 13 14 13 15 13 12 16 17 16 18 16 12 1 19 20 21 20 22 20 19 23 24 23 25 23 19. The main advantage of this path is that highly entangled orbitals located close to the center of the network are optimized several times

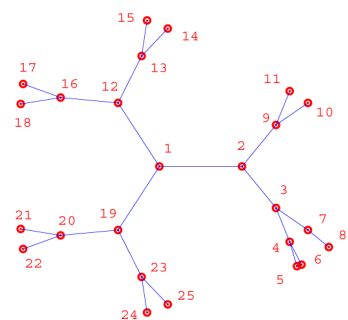


Figure 15. The figure shows how the tree network is traversed through in a full sweep.

in a full sweep. The relative error of the two $^1\Sigma^+$ states as a function of iteration steps obtained by the TTNS method with $z_i = 3$ and $D = 4$ is shown in Figure 16. It can be seen that the

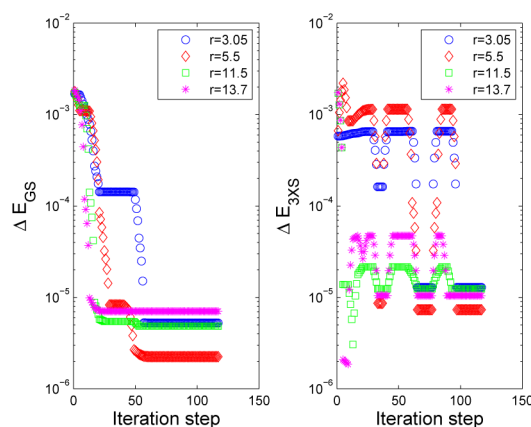


Figure 16. Similar to Figure 14 but for the TTNS method with $z = 3$.

relative error of the ground state energy reached the saturation value of the MPS calculation (shown in Figure 14) after a few iteration steps. However, unlike the MPS result the error dropped further for subsequent iteration steps until a much lower saturation value was reached. The overall improvement compared to the MPS case was almost 2 orders of magnitude. Similar improvement was observed for the excited state, although, due to the low bond dimension the target state was lost again for certain interaction steps, i.e., for certain network configurations.

C. Locating Avoided Crossing by Entanglement. Since the one- and two-orbital entropy functions were calculated to optimize network topologies, they can also be used to locate the avoided crossing. For problems in condensed matter physics the one- and two-orbital entropy functions and the block entropy are used to locate quantum phase transitions.^{56,57} For translationally invariant systems the single-orbital entropy function is the same for all sites, while in a chemical system it is orbital dependent. Therefore, the behavior of I_{tot} as a function of bond length can be used to detect and locate transition points where the wave function changes dramatically. In Figure 17 I_{tot} is shown as a function of bond length. It can be seen that I_{tot} has a cusp-like structure at $r = 11.86$ indicating the position of the avoided crossing.

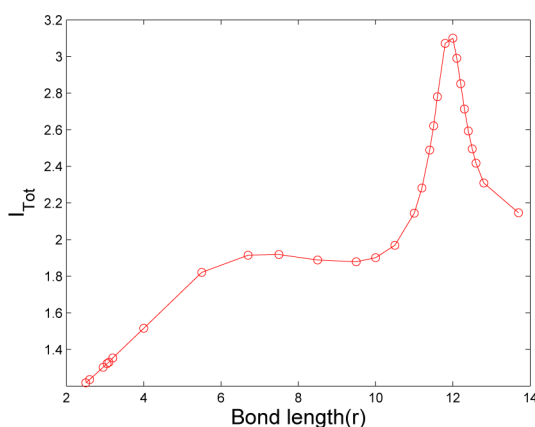


Figure 17. Total quantum information encoded in the wave function as a function bond length. The cusp-like structure indicates the dramatic change in the wave function.

IV. CONCLUSION

The present paper has been devoted to the application of the quantum-chemistry tree tensor network state (QC-TTNS) method to calculate the potential energy curve in the vicinity of the ionic–covalent avoided crossing in LiF. We have discussed the main features of the most general version of the QC-TTNS algorithm in which the local properties of the tensors can be different for each orbital. The optimized tensor topologies, which reflect the structure of the entanglement bonds between the molecular orbitals, were determined by minimizing the entanglement length in the system as the bond length between the Li and F was stretched. In order to compare tensor topology effects only, we have kept all parameters of the algorithms fixed and used a very small bond dimension or alternatively a very small number of block states. By comparing the MPS(DMRG) and TTNS convergence properties we have demonstrated that the TTNS approach can converge to a significantly lower energy. Although the tensor contraction scales as D^{z+1} , the TTNS topology offers a more optimal network structure since the number of components with $z_i = 1$ lying on the boundary scales exponentially with the system size. As a consequence we have found that the relative error of the energy of the ground state as well as the excited states can be improved by an order of magnitude or more for the same value of D . This also indicates that the MPS result can be reproduced with a significantly lower bond dimension using the TTNS method.

Our QC-TTNS approach seems to be a promising direction reflected by the stability and fast convergence of the new method even for systems in which the wave function character changes as a function of bond length, especially in the region of an avoided crossing. The underlying benefits of TTNS is, however, far from fully exploited and the optimization of the method is far more complicated. Due to the more advanced topology, several optimization tasks and problems arise which do not have counterparts in the MPS formulation.

Extension of this work using more complex systems and orbital dependent coordination number is under progress.

AUTHOR INFORMATION

Corresponding Author

*E-mail: olegeza@szfki.hu.

Notes

The authors declare no competing financial interest.

ACKNOWLEDGMENTS

This research was supported by the European Research Area Chemistry (ERA-Chemistry) in part by the Hungarian Research Fund (OTKA) under Grant No. NN110360 and K100908, the DFG SCHN 530/9-1 project under Grant No. 10041620 and FWF-E1243-N19. V.M. and F.V. acknowledge support from the SFB-ViCoM project. Ö.L. acknowledges support from the Alexander von Humboldt foundation and from ETH Zürich during his time as a visiting professor. We are also grateful to Z. Rolik (Budapest) for providing his FCI code based on the CI algorithm of Olsen et al.⁴⁸

REFERENCES

- (1) White, S. R. Density matrix formulation for quantum renormalization groups. *Phys. Rev. Lett.* **1992**, *69*, 2863–2866.
- (2) White, S. R.; Martin, R. L. Ab initio quantum chemistry using the density matrix renormalization group. *J. Chem. Phys.* **1999**, *110*, 4127–4130.
- (3) Legeza, Ö.; Röder, J.; Hess, B. A. QC-DMRG study of the ionic-neutral curve crossing of LiF. *Mol. Phys.* **2003**, *101*, 2019–2028.
- (4) Chan, G. K.-L.; Kállay, M.; Gauss, J. State-of-the-art density matrix renormalization group and coupled cluster theory studies of the nitrogen binding curve. *J. Chem. Phys.* **2004**, *121*, 6110–6116.
- (5) Moritz, G.; Hess, B. A.; Reiher, M. Convergence behavior of the density-matrix renormalization group algorithm for optimized orbital orderings. *J. Chem. Phys.* **2005**, *122*, 024107.
- (6) Moritz, G.; Wolf, A.; Reiher, M. Relativistic DMRG calculations on the curve crossing of cesium hydride. *J. Chem. Phys.* **2005**, *123*, 184105.
- (7) Kurashige, Y.; Yanai, T. High-performance ab initio density matrix renormalization group method: Applicability to large-scale multireference problems for metal compounds. *J. Chem. Phys.* **2009**, *130*, 234114.
- (8) Boguslawski, K.; Tecmer, P.; Barcza, G.; Legeza, Ö.; Reiher, M. Orbital Entanglement in Bond-Formation Processes. *J. Chem. Theory Comput.* **2013**, *9*, 2959–2973.
- (9) Legeza, Ö.; Noack, R.; Sólyom, J.; Tincani, L. In *Computational Many-Particle Physics*; Fehske, H., Schneider, R., Weiße, A., Eds.; Lecture Notes in Physics; Springer: Berlin, Heidelberg, 2008; Vol. 739; pp 653–664.
- (10) Marti, K. H.; Reiher, M. The Density Matrix Renormalization Group Algorithm in Quantum Chemistry. *Z. Phys. Chem.* **2010**, *224*, 583–599.
- (11) Chan, G. K.-L.; Sharma, S. The Density Matrix Renormalization Group in Quantum Chemistry. *Annu. Rev. Phys. Chem.* **2011**, *62*, 465–481.
- (12) Legeza, Ö.; Sólyom, J. Optimizing the density-matrix renormalization group method using quantum information entropy. *Phys. Rev. B* **2003**, *68*, 195116.
- (13) Legeza, Ö.; Sólyom, J. Quantum data compression, quantum information generation, and the density-matrix renormalization-group method. *Phys. Rev. B* **2004**, *70*, 205118.
- (14) Rissler, J.; Noack, R. M.; White, S. R. Measuring orbital interaction using quantum information theory. *Chem. Phys.* **2006**, *323*, 519–531.
- (15) Barcza, G.; Legeza, Ö.; Marti, K. H.; Reiher, M. Quantum-information analysis of electronic states of different molecular structures. *Phys. Rev. A* **2011**, *83*, 012508.
- (16) Boguslawski, K.; Tecmer, P.; Legeza, Ö.; Reiher, M. Entanglement Measures for Single- and Multireference Correlation Effects. *J. Phys. Chem. Lett.* **2012**, *3*, 3129–3135.
- (17) Kurashige, Y.; Chan, G. K.-L.; Yanai, T. Entangled quantum electronic wavefunctions of the Mn_4CaO_5 cluster in photosystem II. *Nat. Chem.* **2013**, *5*, 660–666.

- (18) Östlund, S.; Rommer, S. Thermodynamic Limit of Density Matrix Renormalization. *Phys. Rev. Lett.* **1995**, *75*, 3537–3540.
- (19) Verstraete, F.; Murg, V.; Cirac, J. Matrix product states, projected entangled pair states, and variational renormalization group methods for quantum spin systems. *Adv. Phys.* **2008**, *57*, 143–224.
- (20) Schollwöck, U. The density-matrix renormalization group in the age of matrix product states. *Ann. Phys.* **2011**, *326*, 96–192.
- (21) Haegeman, J.; Osborne, T. J.; Verstraete, F. Post-matrix product state methods: To tangent space and beyond. *Phys. Rev. B* **2013**, *88*, 075133.
- (22) Verstraete, F.; Cirac, J. I. Renormalization algorithms for Quantum-Many Body Systems in two and higher dimensions. *arXiv* **2004**, 0407066.
- (23) Murg, V.; Verstraete, F.; Cirac, J. I. Variational study of hard-core bosons in a two-dimensional optical lattice using projected entangled pair states. *Phys. Rev. A* **2007**, *75*, 033605.
- (24) Murg, V.; Verstraete, F.; Cirac, J. I. Exploring frustrated spin systems using projected entangled pair states. *Phys. Rev. B* **2009**, *79*, 195119.
- (25) Vidal, G. Class of Quantum Many-Body States That Can Be Efficiently Simulated. *Phys. Rev. Lett.* **2008**, *101*, 110501.
- (26) Changlani, H. J.; Kinder, J. M.; Umrigar, C. J.; Chan, G. K.-L. Approximating strongly correlated wave functions with correlator product states. *Phys. Rev. B* **2009**, *80*, 245116.
- (27) Marti, K. H.; Bauer, B.; Reiher, M.; Troyer, M.; Verstraete, F. Complete-graph tensor network states: a new fermionic wave function ansatz for molecules. *New J. Phys.* **2010**, *12*, 103008.
- (28) Marti, K. H.; Reiher, M. New electron correlation theories for transition metal chemistry. *Phys. Chem. Chem. Phys.* **2011**, *13*, 6750–6759.
- (29) Legeza, Ö.; Rohwedder, T.; Schneider, R. In *Encyclopedia of Applied and Computational Mathematics*; Engquist, B. et al., Eds.; Springer: 2013.
- (30) Legeza, Ö.; Rohwedder, T.; Schneider, R.; Szalay, S. In *Many-Electron Approaches in Physics, Chemistry and Mathematics*; Bach, V., Delle Site, L., Eds.; Mathematical Physics Studies; Springer International Publishing: 2014; pp 53–76.
- (31) Hackbusch, W. *Tensor spaces and numerical tensor calculus*; Springer series in computational mathematics; Springer: Heidelberg, 2012; Vol. 42; pp xxiv, 500.
- (32) Orús, R. A practical introduction to tensor networks: Matrix product states and projected entangled pair states. *Ann. Phys.* **2014**, *349*, 117–158.
- (33) Murg, V.; Verstraete, F.; Legeza, Ö.; Noack, R. M. Simulating strongly correlated quantum systems with tree tensor networks. *Phys. Rev. B* **2010**, *82*, 205105.
- (34) Nakatani, N.; Chan, G. K.-L. Efficient tree tensor network states (TTNS) for quantum chemistry: Generalizations of the density matrix renormalization group algorithm. *J. Chem. Phys.* **2013**, *138*, 134113.
- (35) Shi, Y.-Y.; Duan, L.-M.; Vidal, G. Classical simulation of quantum many-body systems with a tree tensor network. *Phys. Rev. A* **2006**, *74*, 022320.
- (36) Tagliacozzo, L.; Evenbly, G.; Vidal, G. Simulation of two-dimensional quantum systems using a tree tensor network that exploits the entropic area law. *Phys. Rev. B* **2009**, *80*, 235127.
- (37) Corboz, P.; Vidal, G. Fermionic multiscale entanglement renormalization ansatz. *Phys. Rev. B* **2009**, *80*, 165129.
- (38) Corboz, P.; Evenbly, G.; Verstraete, F.; Vidal, G. Simulation of interacting fermions with entanglement renormalization. *Phys. Rev. A* **2010**, *81*, 010303.
- (39) Legeza, Ö.; Röder, J.; Hess, B. A. Controlling the accuracy of the density-matrix renormalization-group method: The dynamical block state selection approach. *Phys. Rev. B* **2003**, *67*, 125114.
- (40) McCulloch, I. P. From density-matrix renormalization group to matrix product states. *J. Stat. Mech.* **2007**, 2007, P10014.
- (41) Tóth, A. I.; Moca, C. P.; Legeza, Ö.; Zaránd, G. Density matrix numerical renormalization group for non-Abelian symmetries. *Phys. Rev. B* **2008**, *78*, 245109.
- (42) Zgid, D.; Nooijen, M. On the spin and symmetry adaptation of the density matrix renormalization group method. *J. Chem. Phys.* **2008**, *128*, 014107.
- (43) Sharma, S.; Chan, G. K.-L. Spin-adapted density matrix renormalization group algorithms for quantum chemistry. *J. Chem. Phys.* **2012**, *136*, 124121.
- (44) Wouters, S.; Poelmans, W.; Ayers, P. W.; Neck, D. V. CheMPS2: A free open-source spin-adapted implementation of the density matrix renormalization group for ab initio quantum chemistry. *Comput. Phys. Commun.* **2014**, *185*, 1501–1514.
- (45) Schollwöck, U. The density-matrix renormalization group. *Rev. Mod. Phys.* **2005**, *77*, 259–315.
- (46) Bauschlicher, C. W.; Langhoff, S. R. Full configuration-interaction study of the ionic-neutral curve crossing in LiF. *J. Chem. Phys.* **1988**, *89*, 4246–4254.
- (47) Gordon, M. S.; Schmidt, M. W. In *Theory and Applications of Computational Chemistry*; Dykstra, C. E., Frenking, G., Kim, K. S., Scuseria, G. E., Eds.; Elsevier: Amsterdam, 2005; pp 1167 – 1189.
- (48) Olsen, J.; Roos, B. Ö.; Jørgensen, P.; Jensen, H. J. A. Determinant based configuration interaction algorithms for complete and restricted configuration interaction spaces. *J. Chem. Phys.* **1988**, *89*, 2185–2192.
- (49) Lubich, C.; Rohwedder, T.; Schneider, R.; Vandereycken, B. Dynamical Approximation by Hierarchical Tucker and Tensor-Train Tensors. *SIAM J. Matrix Anal. Appl.* **2013**, *34*, 470–494.
- (50) Xiang, T. Density-matrix renormalization-group method in momentum space. *Phys. Rev. B* **1996**, *53*, R10445–R10448.
- (51) Tecmer, P.; Boguslawski, K.; Legeza, Ö.; Reiher, M. Unravelling the quantum-entanglement effect of noble gas coordination on the spin ground state of CUO. *Phys. Chem. Chem. Phys.* **2014**, *16*, 719–727.
- (52) Legeza, Ö.; Gebhard, F.; Rissler, J. Entanglement production by independent quantum channels. *Phys. Rev. B* **2006**, *74*, 195112.
- (53) Berkman, O.; Vishkin, U. Recursive Star-Tree Parallel Data Structure. *SIAM J. Comput.* **1993**, *22*, 221–242.
- (54) Fiedler, M. Algebraic connectivity of graphs. *Czech. Math. J.* **1973**, *23*, 298–305.
- (55) Fiedler, M. A property of eigenvectors of nonnegative symmetric matrices and its application to graph theory. *Czech. Math. J.* **1975**, *25*, 619–633.
- (56) Legeza, Ö.; Sólyom, J. Two-Site Entropy and Quantum Phase Transitions in Low-Dimensional Models. *Phys. Rev. Lett.* **2006**, *96*, 116401.
- (57) Legeza, Ö.; Sólyom, J.; Tincani, L.; Noack, R. M. Entropic Analysis of Quantum Phase Transitions from Uniform to Spatially Inhomogeneous Phases. *Phys. Rev. Lett.* **2007**, *99*, 087203.